The Attractiveness of the Ternary Rh-Pd-Pt Alloys for CO Oxidation Process

Authors:

Aleksey A. Vedyagin, Yury V. Shubin, Roman M. Kenzhin, Pavel E. Plyusnin, Vladimir O. Stoyanovskii

Date Submitted: 2020-12-17

Keywords: catalytic activity, phase diagram, thermolysis, single precursor, synthesis, ternary alloys

Abstract:

Ternary alloys of platinum group metals attract a growing interest due to their unique catalytic properties. The present research is aimed to synthesize a series of Rh-Pd-Pt alloys with varied ratios of metals using a single-source precursor approach. Rhodium and palladium are partly miscible metals, while each of these metals is unlimitedly miscible with platinum. Thermolysis of complex salts used as a precursor results in the formation of metastable systems. The 3D nanostructure alloys are being formed after the complete decomposition of the single-source precursor. High-resolution transmission electron microscopic studies have shown that the nanoalloys are composed of interconnected polycrystalline ligaments with a mean diameter of 50 nm. The single-phase composition is confirmed by an X-ray diffraction analysis. The ratio of metals plays an important role in determining the catalytic activity of alumina-supported alloys and their thermal stability. According to UV-vis spectroscopy data, the higher palladium portion corresponds to worse dispersion of initially prepared, fresh catalysts. Treatment of the catalysts under prompt thermal aging conditions (up to 800 °C) causes redispersion of palladium-rich alloyed nanoparticles, thus leading to improved catalytic activity and thermal stability.

Record Type: Published Article

Submitted To: LAPSE (Living Archive for Process Systems Engineering)

Citation (overall record, always the latest version):	LAPSE:2020.1203
Citation (this specific file, latest version):	LAPSE:2020.1203-1
Citation (this specific file, this version):	LAPSE:2020.1203-1v1

DOI of Published Version: https://doi.org/10.3390/pr8080928

processes

MDPI

Article

The Attractiveness of the Ternary Rh-Pd-Pt Alloys for CO Oxidation Process

Aleksey A. Vedyagin [1,*], Yury V. Shubin [2], Roman M. Kenzhin [1], Pavel E. Plyusnin [2] and Vladimir O. Stoyanovskii [1]

1 Boreskov Institute of Catalysis SB RAS, Department of Materials Science and Functional Materials, 630090 Novosibirsk, Russia; romankenzhin@catalysis.ru (R.M.K.); stoyn@catalysis.ru (V.O.S.)
2 Nikolaev Institute of Inorganic Chemistry SB RAS, Department of Chemistry of Coordination, Cluster and Supramolecular Compounds, 630090 Novosibirsk, Russia; shubin@niic.nsc.ru (Y.V.S.); plus@niic.nsc.ru (P.E.P.)
* Correspondence: vedyagin@catalysis.ru

Received: 8 July 2020; Accepted: 30 July 2020; Published: 2 August 2020

Abstract: Ternary alloys of platinum group metals attract a growing interest due to their unique catalytic properties. The present research is aimed to synthesize a series of Rh-Pd-Pt alloys with varied ratios of metals using a single-source precursor approach. Rhodium and palladium are partly miscible metals, while each of these metals is unlimitedly miscible with platinum. Thermolysis of complex salts used as a precursor results in the formation of metastable systems. The 3D nanostructure alloys are being formed after the complete decomposition of the single-source precursor. High-resolution transmission electron microscopic studies have shown that the nanoalloys are composed of interconnected polycrystalline ligaments with a mean diameter of 50 nm. The single-phase composition is confirmed by an X-ray diffraction analysis. The ratio of metals plays an important role in determining the catalytic activity of alumina-supported alloys and their thermal stability. According to UV-vis spectroscopy data, the higher palladium portion corresponds to worse dispersion of initially prepared, fresh catalysts. Treatment of the catalysts under prompt thermal aging conditions (up to 800 °C) causes redispersion of palladium-rich alloyed nanoparticles, thus leading to improved catalytic activity and thermal stability.

Keywords: ternary alloys; synthesis; single precursor; thermolysis; phase diagram; catalytic activity

1. Introduction

Currently, a growing interest is attracted by metallic nanoparticles consisting of two and more metals with a specified interaction between them. Such nano-objects exhibit unique properties in various fields of application [1–7]. Thereby, one of the actual challenges of modern materials science is the development of the preparation routes to obtain metallic nanoparticles with a predefined size, composition, and, finally, properties. Among the variety of metals efficiently used in catalytic processes, precious metals of platinum group (Pt, Pd, and Rh) are of special importance. The palladium-based catalysts are known as highly active and efficient in a wide range of heterogeneous reactions starting from fine organic synthesis to partial and complete oxidation, selective hydrogenation or dehydrogenation [8–21]. For instance, being deposited on oxide supports (ceria, zirconia, alumina, etc.), Pd provides complete oxidation of hydrocarbons and CO that makes it a significant component of the modern catalysts of the engine exhaust gases purification [22–29]. Platinum is widely applied in numerous industrially important catalytic processes including hydrogenation (hydrogenation of C=C, C=O, N=O, and C≡N bonds), dehydrogenation (cleavage of N-H and C-H bonds), reforming of oxygenates (alcohols, polyols, and other), CO oxidation, water gas shift reaction, conversion of CH_4,

hydrodechlorination, as well as in fuel cells [30–38]. Rhodium is famous due to its ability to activate and reduce nitrogen oxides. This feature made it to be another essential component of the onboard emission control systems [39]. Along with this, Rh can catalyze the most of the reactions traditionally performed over Pd and Pt catalysts [40–48].

All these metals were recently reported to show a synergetic effect in terms of activity and/or stability being alloyed with other metals. Most often, bimetallic systems are used for this purpose. Thus, the oxidative function of palladium can be noticeably enhanced by modifying with Ni, Fe, Cr, Cu, Co, Ag, etc. [49–55]. Platinum catalysts were doped with Ni, Au, and Cu [6,30,56,57]. Alloying of palladium and platinum with rhodium was numerously reported to improve the thermal stability of the catalysts and widen their functionality [58–68]. It is important to note that Pd and Rh are partly miscible metals [69]. Their miscibility diagram is represented by a large gap, and the thermodynamically stable alloys cannot exist within this immiscibility area. As it was shown recently, the Pd/Rh ratio in the alloy plays an important role in catalytic behavior of the alumina-supported catalysts [70]. The highest resistance towards high-temperature aging was exhibited by the system with the Pd/Rh ratio of 3/2. Moreover, this ratio affects the mechanism of the oxidation/reduction reactions taking place. A decrease in the rhodium portion diminishes the involvement of NO species into oxidation of hydrocarbons. The best performance corresponds to the mentioned area of immiscibility when the Pd-Rh alloy is metastable. To prepare securely the metastable alloys, a single precursor concept is shown to be the most efficient [68,71]. Platinum is miscible with both metals without any limits, and there are no problems to synthesize bimetallic Pt-Pd or Pt-Rh alloys with any desired ratio.

During the last decades, ternary alloyed systems, containing Pd, Pt, and Rh, attract more and more attention of the research [43,72–81]. The synergistically improved efficiency was proved for the selective catalytic oxidation of ammonia, oxidation of hydrocarbons, including substituted ones, and oxidation of CO. Thereby, ternary Pt-Pd-Rh alloys are the perspective to be used in three-way catalysts. It should be noted that each of these metals being supported on oxide carriers is characterized by specific behavior at elevated temperatures. Palladium species undergo surface migration and agglomeration into relatively large particles [82]. Rhodium ions can diffuse into the bulk of the alumina support, where they initiate local phase transformations leading to the formation of the corundum phase [83]. Both these processes are responsible for the deactivation of catalysts. At the same time, agglomeration of palladium can be considered as a reversible process, since at temperatures of 800 °C formed Pd (PdO) particles can undergo redispersion, [84–88] while for rhodium ions the deactivation is irreversible due to their encapsulation inside the α-Al_2O_3 phase. Alloying of Pd with Rh helps to prevent both these deactivation processes. Platinum is the most tolerant metal towards high-temperature aging among the considered trio [89]. In the case when all the metals are alloyed together, high-temperature treatment faces another problem of their segregation. Liu et al. have reported that platinum and palladium atoms prefer to segregate on the surface of the alloyed nanoparticle, while rhodium atoms tend to aggregate inside [80]. Palladium atoms are characterized by stronger surface segregation if compare with platinum ones. Enrichment of the surface of bimetallic Pd-Rh and trimetallic Pt-Pd-Rh alloys was theoretically justified by Chen et al. using the modified analytical embedded atom method combined with Monte Carlo computer simulations [74]. In the case of ternary alloy, the surface Pd concentration is influenced by bulk Rh compositions.

Taking into account all the trends existing in the literature, the present research aims to synthesize the ternary $Rh_2(Pd_xPt_{1-x})_3$ alloys with varied Pd/Pt ratio using a single precursor approach and study the physicochemical properties, catalytic activity in CO oxidation and thermal stability at elevated temperatures. The phase composition of the prepared samples is examined using an X-ray diffraction analysis. Catalytic activity and thermal stability are studied in a prompt thermal aging regime [90]. The state of palladium in fresh and aged catalysts is estimated using UV-vis spectroscopy.

2. Materials and Methods

2.1. Synthesis of Precursors

In the present work, single-source precursors $[RhEn_3]_2[Pd(NO_2)_4]_3$, $[RhEn_3]_2[Pt(NO_2)_4]_3$, and $[RhEn_3]_2[Pd_xPt_{1-x}(NO_2)_4]_3$, where En is ethylenediamine $C_2H_8N_2$, were synthesized according to the following procedures.

$[RhEn_3]_2[Pd(NO_2)_4]_3$: 4 mL of $K_2[Pd(NO_2)_4]$ aqueous solution (623 mg, 1.5 mmol) was added to 3 mL of $[RhEn_3]Cl_3{\cdot}3H_2O$ aqueous solution (500 mg, 1 mmol) at continuous stirring. The sediment was filtered using a porous glass filter, washed with 3 mL of ice water and 5 mL of ethanol. The yield of the double complex salt was 63% (450 mg).

$[RhEn_3]_2[Pt(NO_2)_4]_3$: 8 mL of $K_2[Pt(NO_2)_4]$ aqueous solution (533.2 mg, 1.1 mmol) was added to 2 mL of $[RhEn_3]Cl_3{\cdot}3H_2O$ aqueous solution (312.4 mg, 0.7 mmol) at continuous stirring. The sediment was filtered and washed as described above. The yield of the double complex salt was 67% (200 mg).

The double complex salts containing three metals were obtained by mixing of $[RhEn_3]Cl_3{\cdot}3H_2O$ aqueous solution with a joint solution of $K_2[Pt(NO_2)_4]$ and $K_2[Pd(NO_2)_4]$ taken in an appropriate ratio. For instance, $[RhEn_3]_2[Pd_{0.5}Pt_{0.5}(NO_2)_4]_3$ was prepared by mixing 3 mL of $K_2[Pt(NO_2)_4]$ aqueous solution (145.87 mg, 0.29 mmol) and 3 mL of $K_2[Pd(NO_2)_4]$ aqueous solution (117.6 mg, 0.29 mmol) with 1 mL of $[RhEn_3]Cl_3{\cdot}3H_2O$ aqueous solution (169.5 mg, 0.38 mmol) at continuous stirring. The sediment was filtered and washed as described above. The yield of the double complex salt was 44% (130 mg).

2.2. Synthesis of Catalysts

The samples for the catalytic testing were prepared by an incipient wetness impregnation of commercial alumina powder (Puralox TH 100/150; Sasol, Germany) with aqueous solutions of the double complex salts at room temperature under continuous stirring. Then, the samples undergo drying at 105 °C for 12 h and calcination at 400 °C for 1 h. The total metal loading of Pt, Pd, and Rh was 0.2 wt %. The ratio of (Pd+Pt)/Rh was 3/2, while the Pd/Pt ratio was varied as 3/1, 1/1, and 1/3. The resulting samples were marked as $Rh_2(Pd_{0.75}Pt_{0.25})_3/\gamma\text{-}Al_2O_3$, $Rh_2(Pd_{0.5}Pt_{0.5})_3/\gamma\text{-}Al_2O_3$, and $Rh_2(Pd_{0.25}Pt_{0.75})_3/\gamma\text{-}Al_2O_3$. The reference samples $Pd/\gamma\text{-}Al_2O_3$, $Pt/\gamma\text{-}Al_2O_3$, $Rh_2Pd_3/\gamma\text{-}Al_2O_3$, and $Rh_2Pt_3/\gamma\text{-}Al_2O_3$ were obtained by similar procedures.

2.3. Characterization Techniques

The powder X-ray diffraction (XRD) analysis of the prepared precursors and alloys was performed at room temperature and atmospheric pressure on a Shimadzu XRD-7000 diffractometer (Shimadzu Corp., Kyoto, Japan) operating with CuK_α radiation, nickel filter in reflected beam, and scintillation detector with amplitude discrimination. The data were collected step-by-step in the range of angles 2θ = 5–135° with a step of 0.05°. The resulting patterns were analyzed and fitted using a PowerCell 2.4 and WINFIT 1.2.1 software packages, correspondingly [91,92]. The obtained coordination compounds were single-phase, which was identified by indexing the powder XRD patterns similarly to theoretical patterns for complexes studied by an X-ray structure analysis.

Elemental (C, H, and N) analysis was carried out on a Euro EA 3000 analyzer (Eurovector, S.p.a., Milan, Italy). The specimen was thermally destroyed in the presence of solid oxidizers with the addition of gaseous oxygen until the quantitative formation of final products: CO_2, water, and nitrogen. The obtained gas mixture was separated chromatographically. The quantities of the components were used to calculate the portions (wt %) of carbon, hydrogen, and nitrogen in the analyzed sample.

The metal content in the samples was determined by the atomic absorption method using a Hitachi Z-800 spectrometer (Hitachi, Tokyo, Japan). The sample was dissolved in aqua regia, evaporated until the minimal volume, loaded into a graduated flask and diluted by distilled water until marker.

All the theoretical values of the element's content were calculated from the molecular weights of the coordination compounds.

The metal loading in the supported catalysts was measured by an energy dispersive X-ray fluorescence (ED XRF) analysis. An M1 MISTRAL spectrometer (Bruker Nano Nano GmbH, Berlin, Germany) with a microfocus X-ray tube (W-anode) and a high-resolution silicon drift detector (SDD, energy resolution <150 eV at Mn-K_α) was used.

Thermogravimetric analyses (TGA) were carried out using a TG 209 F1 Iris thermobalance (NETZSCH-Gerätebau GmbH, Selb, Germany). Synchronic thermal analysis was performed using an STA 449F1 Jupiter analyzer equipped with a QMS 403D Aëolos quadrupole mass spectrometer (NETZSCH-Gerätebau GmbH, Selb, Germany). The measurements were made in a hydrogen–helium mixture (10% vol. H_2 in He). The parameters of the TGA experiments were the following: sample weight of 20 mg; Al-crucibles; the gas flow rate of 60 mL/min; and the temperature ramping rate of 10 °C/min.

The high-resolution transmission electron microscopy (HR TEM) measurements were performed using a JEM-2010 electron microscope (JEOL Ltd., Tokyo, Japan) with lattice plane resolution 0.14 nm at an accelerating voltage of 200 kV. Images of periodic structures were analyzed by the Fourier method. A local energy-dispersive X-ray analysis (EDXA) was carried out using an EDX spectrometer Xflash (Bruker Nano GmbH, Berlin, Germany) fitted with a Si detector with a resolution of 128 eV. The samples for the HR TEM study were prepared on a perforated carbon film mounted on a copper grid.

Diffuse reflectance UV-Vis spectra were recorded between 200 and 850 nm using a UV-vis spectrometer UV-VIS 2501 PC (Shimadzu Corp., Kyoto, Japan) with IRS-250A diffusion reflection attachment. The UV-vis spectra were transformed into the Kubelka–Munk function F(R) calculated as $F(R) = (1 - R)^2/2R$, where R is the experimentally measured reflectivity coefficient of the samples [93].

2.4. Testing the Catalytic Activity in the Oxidation of CO

The catalytic performance of the alumina-supported catalysts was examined in a model reaction of CO oxidation. Each sample was studied in seven consecutive cycles under prompt thermal aging (PTA) conditions as described elsewhere [90,93–96]. The testing procedure was as follows. The sample (300 mg) was loaded into the quartz flow reactor, and then the reaction mixture contained 0.15 vol% CO, 14.0 vol% O_2, 0.01 vol% NO, 0.01 vol% hydrocarbons (a mixture of methane, propylene, and toluene), and nitrogen (as balance) was passed through the reactor. The flow rate was 334 mL/min. A temperature ramping rate was 10 °C/min. The final temperature of the catalytic cycle was 320 °C for 1st and 2nd cycles, 600 °C for 3rd and 4th cycles, and 800 °C for the last three cycles. The CO concentration at the reactor outlet was registered by a gas analyzer ULTRAMAT 6 (Siemens). The temperature of 50% CO conversion (T_{50}) was used as a criterion to compare the thermal stability of the catalysts.

3. Results and Discussion

3.1. Characterization of the Precursors

At the first step of the study, all the prepared coordination compounds were characterized by elemental analysis, atomic absorption spectroscopy, and infrared spectroscopy. The elemental compositions of $[RhEn_3]_2[Pd(NO_2)_4]_3$, $[RhEn_3]_2[Pt(NO_2)_4]_3$, and $[RhEn_3]_2[Pd_{0.5}Pt_{0.5}(NO_2)_4]_3$ salts are presented in Table 1. The infrared spectra of the prepared coordination compounds are shown in Figure 1a and the corresponding oscillation frequencies are summarized in Table 2. As seen, the measured values of elements content were very close to the calculated ones. The results of the infrared spectroscopy (Table 2) allowed identifying of the functional groups in the compositions of the salts.

Table 1. Elemental composition of the double complex salts.

Precursor	Content (Measured/Calculated), %					
	C	N	H	Pt	Rh	Pd
$[RhEn_3]_2[Pd(NO_2)_4]_3$	9.5/10.02	20.4/23.38	3.1/3.37	-	14.1/14.32	21.2/22.21
$[RhEn_3]_2[Pt(NO_2)_4]_3$	8.4/8.46	19.6/19.73	2.8/2.84	35.0/34.35	12.0/12.08	-
$[RhEn_3]_2[Pd_{0.5}Pt_{0.5}(NO_2)_4]_3$	9.0/9.18	21.3/21.40	3.0/3.08	19.3/18.63	13.3/13.10	9.5/10.16

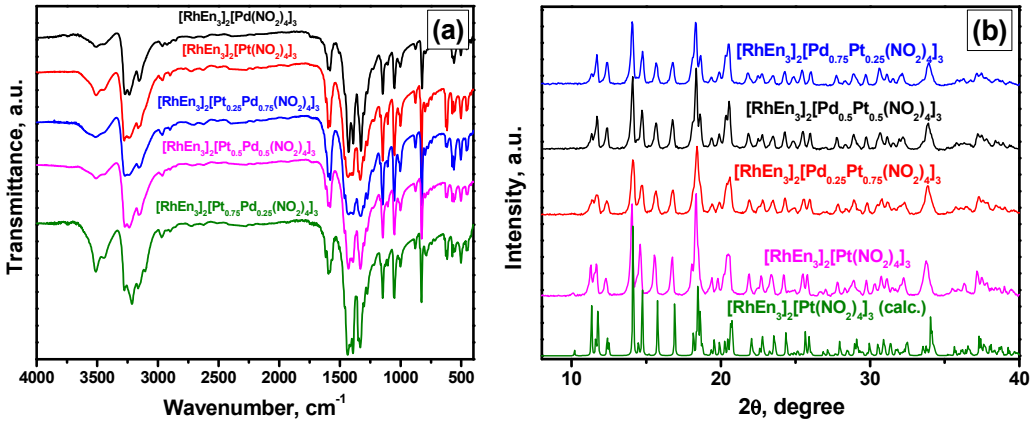

Figure 1. Infrared spectra (**a**) and experimental XRD patterns (**b**) of the prepared complex compounds. The calculated pattern of $[RhEn_3]_2[Pt(NO_2)_4]_3$ is given for comparison.

Table 2. The oscillation frequencies in the infrared spectra of the prepared complex compounds.

Compound	ν_s(NH)	ν(CH)	δ(NH_2)	ν_a(NO_2)	ν(CN)	δ(ONO)
$[RhEn_3]_2[Pd(NO_2)_4]_3$	3271 3237 3153	2965	1581	1428 1390 1327 1299	1050	823
$[RhEn_3]_2[Pt(NO_2)_4]_3$	3278 3234 3161	2962	1597 1582 1146	1432 1394 1331	1049	827
$[RhEn_3]_2[Pd_{0.75}Pt_{0.25}(NO_2)_4]_3$	3271 3237 3153	2964	1597 1581 1145	1428 1391 1328	1050	824
$[RhEn_3]_2[Pd_{0.5}Pt_{0.5}(NO_2)_4]_3$	3273 3237 3147	2964	1596 1581 1145	1429 1393 1330	1050	826
$[RhEn_3]_2[Pd_{0.25}Pt_{0.75}(NO_2)_4]_3$	3275 3236 3148	2963	1597 1582 1146	1431 1394 1332	1050	827

The obtained double complex salts $[RhEn_3]_2[Pd(NO_2)_4]_3$ and $[RhEn_3]_2[Pt(NO_2)_4]_3$ and their solid solutions with varied ratios of metals in the anionic part were easily isolated into the solid phase in the nonaqueous form. Both the purity and the single phase of all the synthesized products were confirmed by an XRD analysis method (Figure 1b). As follows from the figure, the experimental patterns corresponded well with the simulated (calculated) one.

The thermal decomposition of $[RhEn_3]_2[Pd(NO_2)_4]_3$ salt in a hydrogen medium was recently reported in detail [96]. The thermolysis of the double complex salt $[RhEn_3]_2[Pd(NO_2)_4]_3$ and the solid solutions of $[RhEn_3]_2[Pd_xPt_{1-x}(NO_2)_4]_3$ composition in a reductive medium proceeded similarly, in few hardly separable stages accompanied by exothermic effects (Figure 2a). Along with this, the thermal stability of the solid solutions depends on the content of palladium in their composition (Figure 2b). The starting temperature point of decomposition regularly decreased with an increase of the palladium content due to the lower thermal stability of the Pd-containing coordination compounds. The final temperature point of decomposition was not changed noticeably and corresponded to 310–320 °C. The

total weight loss and the weight of the products obtained by pyrolysis in a reductive atmosphere agreed well with the calculated content of metals in the composition of the initial single-source precursors (Table 3).

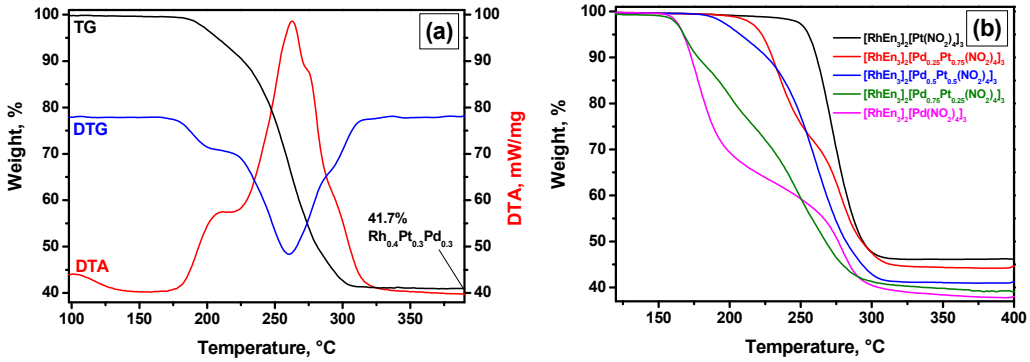

Figure 2. The thermal analysis curves obtained in a reductive medium at a ramping rate of 10 °C/min: (**a**) TG, DTG, and DTA for the $[RhEn_3]_2[Pd_{0.5}Pt_{0.5}(NO_2)_4]_3$ salt and (**b**) TG curves for the solid solutions $[RhEn_3]_2[Pd_xPt_{1-x}(NO_2)_4]_3$.

Table 3. Content of metals in the composition of the prepared complex salts according to the thermal analysis results.

Compound	Measured	Calculated
$[RhEn_3]_2[Pd(NO_2)_4]_3$	36.8%	36.53%
$[RhEn_3]_2[Pd_{0.75}Pt_{0.25}(NO_2)_4]_3$	39.2%	39.33%
$[RhEn_3]_2[Pd_{0.5}Pt_{0.5}(NO_2)_4]_3$	41.7%	41.89%
$[RhEn_3]_2[Pd_{0.25}Pt_{0.75}(NO_2)_4]_3$	44.3%	44.26%
$[RhEn_3]_2[Pt(NO_2)_4]_3$	46.2%	46.43%

3.2. Characterization of the Alloys

Some representative TEM images of the products of the precursors' thermolysis are shown in Figure 3. The decomposition of the precursors in a hydrogen atmosphere along with subsequent heating of the products up to 600 °C resulted in the formation of an alloy characterized by a porous sponge-like structure. In terms of morphology, the nanoporous alloys consisted of interconnecting ligaments with a mean diameter of 50 nm. As evidenced by HR TEM, the ligaments were polycrystalline with grain boundaries separated by a few nanometers.

An energy-dispersive spectroscopic study of the as-prepared samples confirmed that the Rh:Pd:Pt atomic ratio in alloys was consistent with the atomic ratio of metals in the respective precursors. The alloy nature of the porous products was also confirmed by estimation of the interplanar spacing (d_{111}) from the high-resolution TEM images (Figure 3). The estimated mean values of the interplanar spacing correlated satisfactorily with the corresponding d_{111} values calculated from the lattice parameters obtained by the XRD analysis method (Table 4).

It should be noted that the binary systems Pt-Pd, Rh-Pt, and Rh-Pd were characterized by a wide area of existence of the random solid solutions with face-centered cubic cell (fcc, space group Fm3m) [69,97–101]. In all these binary systems the components were miscible at the temperatures above 900 °C in a whole range of compositions. The Rh-Pd system exhibited a miscibility gap with the critical point of solubility at 58 at.% Rh and 820 °C [69].

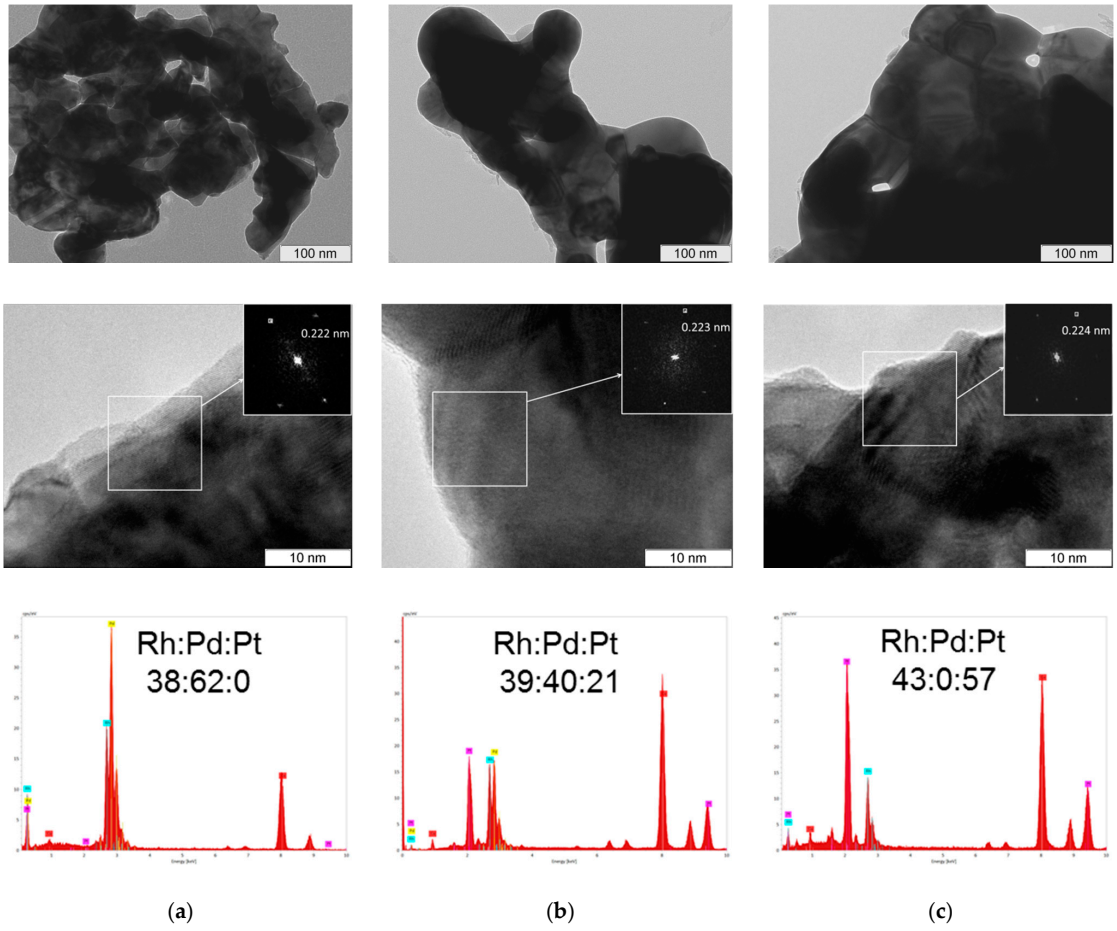

Figure 3. HR TEM images and EDX spectra of the as-prepared nanoalloys. (**a**) Rh_2Pd_3; (**b**) $Rh_2(Pd_{0.50}Pt_{0.50})_3$; and (**c**) Rh_2Pt_3.

Up to date, there is no information concerning an experimental study on the subsolidus area of the ternary Rh-Pd-Pt system. The only exception is the reported isothermal section at 1200 °C illustrating the unlimited miscibility of the components at this temperature in a whole range of compositions [102,103]. Therefore, the hypothetical scheme of the phase diagram for this ternary system can be based on the extrapolations from the binary Pt-Pd, Rh-Pt, and Rh-Pd systems only. Additionally, it should be taken into account that since the binary Rh-Pd alloy separated onto two phases at temperatures below 820 °C, the phase diagram of the ternary system was characterized by a presence of the miscibility gap, which should be based on the Rh-Pd axis. The first attempt to draw the phase diagram for the Rh-Pd-Pt system was undertaken using the calculations of the heats of mixing by the Monte Carlo (MC) method combined with the semi-empirical modified embedded atom method (MEAM). The resulting miscibility gap for the temperature of 327 °C is presented in Figure 4. Taking into account the experimental temperature dependency of the equilibrium solubility of the solid solutions in the Rh–Pd system and the isothermal cross-section of the ternary phase diagram for the Rh-Pd-Pt system at 327 °C, the hypothetical miscibility gaps for the temperatures 600, 700, and 800 °C are drawn in Figure 4. As seen from the presumed ternary phase diagrams, the alloys $Rh_2(Pd_{0.25}Pt_{0.75})_3$, $Rh_2(Pd_{0.5}Pt_{0.5})_3$, and Rh_2Pt_3 at 600 °C and above (filled triangles) were located in a homogeneous area and, therefore, should be in equilibrium. Contrary, the Rh_2Pd_3 and $Rh_2(Pd_{0.75}Pt_{0.25})_3$ alloys at the same temperatures (empty triangles) should be metastable.

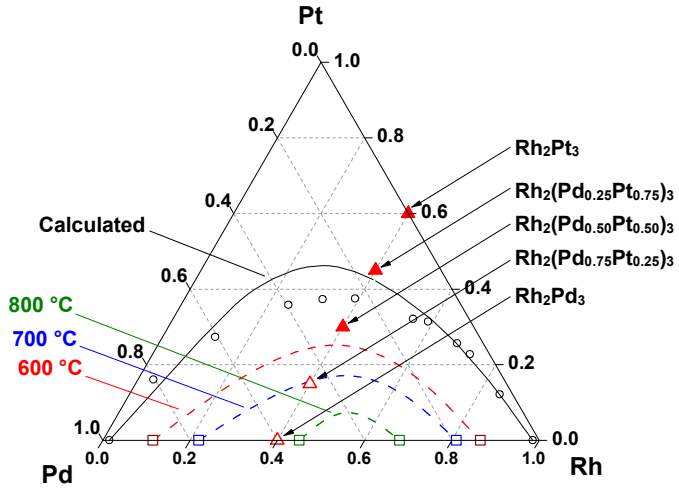

Figure 4. The phase diagram of the Rh-Pd-Pt alloy. The calculated miscibility gap is based on data reported by Luyten et al. [104]. The colored squares correspond to experimental points for the binary Pd-Rh systems at temperatures of 600, 700, and 800 °C, while dash lines show the estimated miscibility gaps for the ternary Rh-Pd-Pt systems at these temperatures. Red triangles are experimental points for the alloys studied in the present work, where filled and empty triangles lie in areas of homogeneity and metastability, accordingly.

Table 4. The ratio of metals and the crystal lattice parameters in the prepared nanoalloys.

Sample	Lattice Parameter, *a*, Å	d_{111} (calc.) **, Å	d_{111} (TEM), Å	Rh:Pd:Pt (EDX)
Rh	3.803 *	2.196	-	-
Pd	3.890 *	2.246	-	-
Pt	3.923 *	2.265	-	-
Rh_2Pd_3	3.856	2.226	2.22	38:62:0
$Rh_2(Pd_{0.75}Pt_{0.25})_3$	3.861	2.229	2.23	37:53:10
$Rh_2(Pd_{0.50}Pt_{0.50})_3$	3.865	2.231	2.23	39:40:21
$Rh_2(Pd_{0.25}Pt_{0.75})_3$	3.87	2.234	2.24	38:22:40
Rh_2Pt_3	3.877	2.238	2.24	43:00:57

* The lattice parameters are taken from the ICDD PDF-2 database [105]; ** The values are calculated from the lattice parameter.

The XRD patterns of the products obtained by the decomposition of the single-source precursors $[RhEn_3]_2[Pd(NO_2)_4]_3$, $[RhEn_3]_2[Pt(NO_2)_4]_3$, $[RhEn_3]_2[Pd_{0.75}Pt_{0.25}(NO_2)_4]_3$, $[RhEn_3]_2[Pd_{0.5}Pt_{0.5}(NO_2)_4]_3$, and $[RhEn_3]_2[Pd_{0.25}Pt_{0.75}(NO_2)_4]_3$ at 600 °C in a hydrogen atmosphere are presented in Figure 5. As seen, they contained only the fcc phase (Figure 5a). The shift in the position of the reflexes regarding pure Pd, Pt, and Rh was observed in a far angle region (Figure 5b). This indicates the formation of homogeneous solid solutions. The analysis of the reflexes position allowed the conclusion that an increase of the Pd content in the ternary alloy composition leads to the shifting of the reflexes towards a far angle region, thus testifying in a decrease in the parameter of the elementary cell of the solid solution. The lattice parameters of the alloys calculated from the positions of 331 and 420 reflexes are summarized in Table 4.

Figure 6 shows the dependencies of the lattice parameters of the alloys on the atomic fraction in the Rh-Pt and Rh-Pd systems based on the literature data [69,101,106]. In these binary systems, an appropriate satisfiability of the Vegard's law was observed. The maximum deviation of the lattice parameters from the law did not exceed 0.002 Å. Taking all these into account, interpolating isotherms 'lattice parameter—composition' for the ternary Rh-Pd-Pt alloys are plotted in Figure 6 (dashed lines).

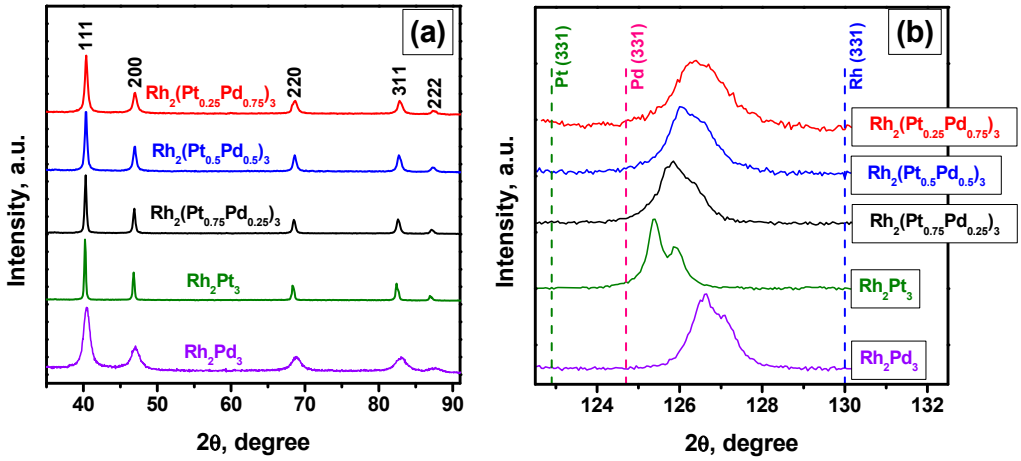

Figure 5. The XRD patterns of the prepared nanoalloys within 2θ ranges of 35–90 ° (**a**) and 123–133 ° (**b**).

The measured values of lattice parameters of the ternary alloys (Figure 6, triangles) matched the corresponding values on the plotted dependencies. Thereby, this confirms a coincidence of the composition of the synthesized homogeneous ternary solid solutions with the composition specified at the synthesis of the single-source precursors.

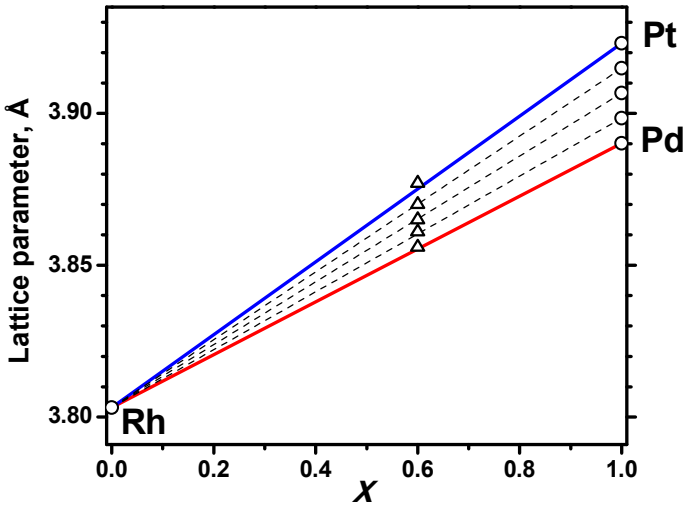

Figure 6. Dependencies of the lattice parameters of the Rh-Pt and Rh-Pd nanoalloys on their composition.

3.3. Characterization and Testing of the Alumina-Supported Catalysts

In the next step of the study, the synthesized precursors were supported on the commercial alumina powder via an incipient wetness impregnation. In order to control the content of the supported metals, the catalysts samples were characterized by an ED XRF method. The measured values along with the calculated ones are summarized in Table 5. As seen, the values coincided with a good enough accuracy.

Table 5. Content of metals in the composition of the alumina-supported catalysts according to the ED XRF results.

Sample	Content (Measured/Calculated), %		
	Rh	**Pd**	**Pt**
Rh_2Pt_3/Al_2O_3	0.05/0.051	-	0.15/0.149
Rh_2Pd_3/Al_2O_3	0.08/0.076	0.12/0.119	-
$Rh_2(Pd_{0.25}Pt_{0.75})_3/Al_2O_3$	0.05/0.057	0.03/0.022	0.11/0.121
$Rh_2(Pd_{0.5}Pt_{0.5})_3/Al_2O_3$	0.05/0.062	0.05/0.048	0.10/0.089
$Rh_2(Pd_{0.75}Pt_{0.25})_3/Al_2O_3$	0.07/0.069	0.08/0.081	0.06/0.049
Pt/Al_2O_3	-	-	0.16/0.15
Pd/Al_2O_3	-	0.11/0.119	-

All the samples of alumina-supported catalysts were tested in a model reaction of CO oxidation. The testing procedure was performed under prompt thermal aging conditions, which allowed monitoring of the degradation of the catalysts during the high-temperature exposure. The corresponding light-off curves are shown in Figure 7a–e. To compare the samples evidently, the dependencies of the T_{50} parameter on the catalytic run number are plotted in Figure 7f. The platinum-only catalyst was used as a reference sample. As follows from the obtained results, the metals in the alloy interacted with each other and influence the catalytic properties of the catalyst as a whole. For instance, $Pt/\gamma\text{-}Al_2O_3$ sample demonstrated poor initial activity (T_{50} = 286 °C) but undergoes reactivation at elevated temperatures. Most significantly this effect became apparent after heating up to 800 °C. In the case of the bimetallic $Rh_2Pt_3/\gamma\text{-}Al_2O_3$ catalyst, the tendencies in catalytic activity and stability remained the same. In general, the presence of rhodium in the catalyst's composition made the catalyst a little bit more active. For the ternary alloy systems, a partial replacement of platinum with palladium much evidently enhanced the initial activity of the catalyst: more Pd content in the alloy corresponded to the lower value of the T_{50} parameter. Since palladium is known to be less stable than platinum, the aging of the catalysts at 600 °C led to their noticeable deactivation. Then, being heated up to 800 °C, $Rh_2(Pd_{0.25}Pt_{0.75})_3/\gamma\text{-}Al_2O_3$ and $Rh_2(Pd_{0.5}Pt_{0.5})_3/\gamma\text{-}Al_2O_3$ catalysts show reactivation similarly to the samples without palladium. Oppositely, the sample $Rh_2(Pd_{0.75}Pt_{0.25})_3/\gamma\text{-}Al_2O_3$ containing a higher amount of Pd continued to deactivate even after treatment at 800 °C. Taking into account the mentioned oppositely directed trends, it could be concluded the most promising system is a ternary alloy $Rh_2(Pd_{0.5}Pt_{0.5})_3$ with an equivalent amount of palladium and platinum. At a higher content of Pd, the "metal–metal" interactions in the alloy were assumed to become weaker due to partial immiscibility of palladium and rhodium, and the further catalytic behavior of the catalyst was determined by Pd. If platinum dominates over palladium, then the catalyst performs worse activity.

As we have reported recently, optical spectroscopy methods are useful and informative tools allowing characterizing of the state of the supported precious metals and their alloys as well as the changes taking place during high-temperature aging [93]. Therefore, all the studied binary and ternary catalysts and the monometallic reference samples were examined by a diffuse reflectance UV-vis spectroscopy. To exclude the effect of "metal–metal" interactions, some additional reference samples obtained by mechanical mixing of corresponding monometallic catalysts were prepared and studied.

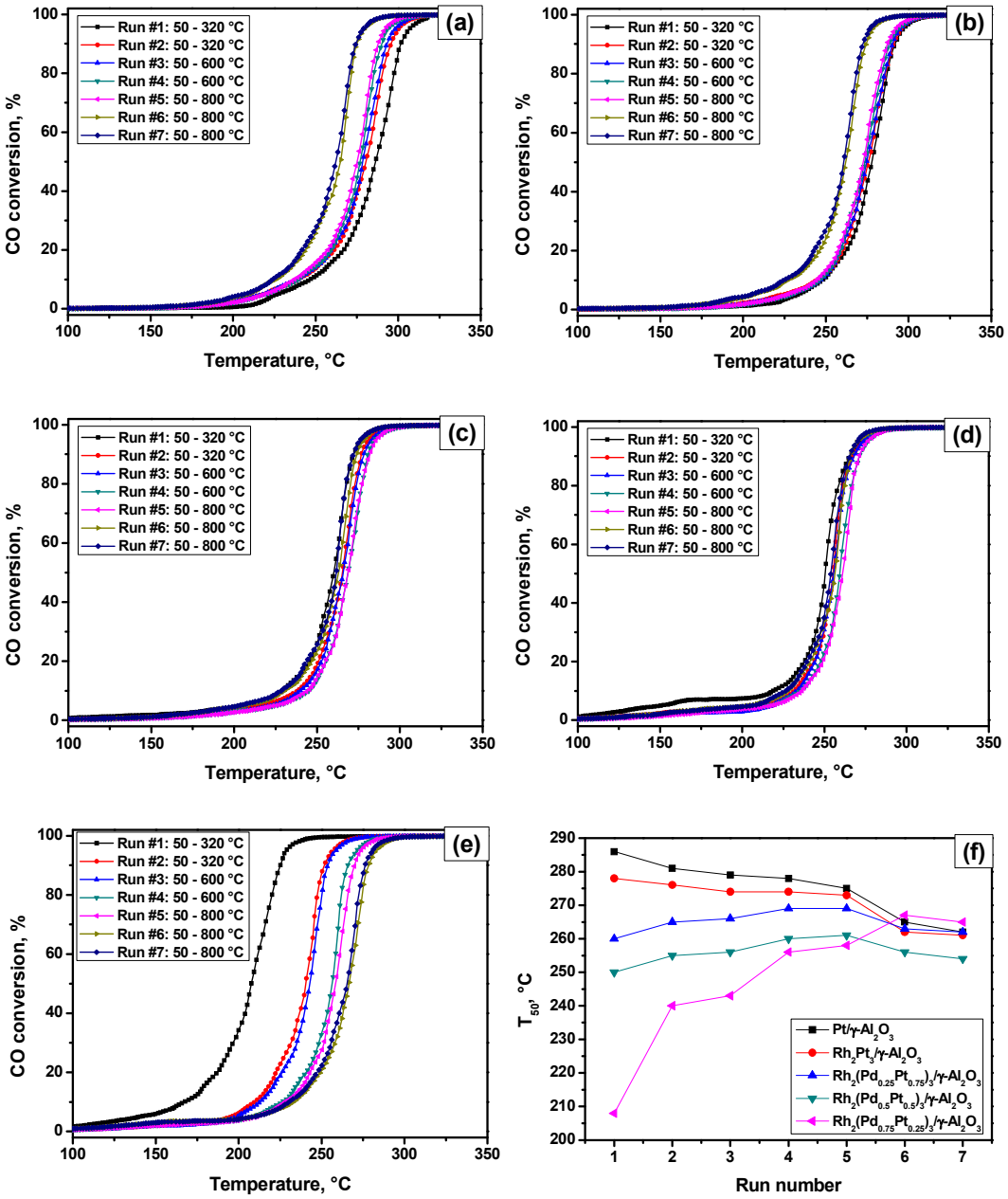

Figure 7. The temperature dependencies of CO conversion under prompt thermal aging (PTA) conditions for the studied samples: (**a**) $Pt/\gamma\text{-}Al_2O_3$; (**b**) $Rh_2Pt_3/\gamma\text{-}Al_2O_3$; (**c**) $Rh_2(Pd_{0.25}Pt_{0.75})_3/\gamma\text{-}Al_2O_3$; (**d**) $Rh_2(Pd_{0.5}Pt_{0.5})_3/\gamma\text{-}Al_2O_3$; and (**e**) $Rh_2(Pd_{0.75}Pt_{0.25})_3/\gamma\text{-}Al_2O_3$. The dependencies of the T_{50} parameter on the run number for the same samples (**f**).

Figure 8 presents the UV-vis spectra for the monometallic $Pt/\gamma\text{-}Al_2O_3$ and $Rh/\gamma\text{-}Al_2O_3$, samples and the bimetallic $Rh_2Pt_3/\gamma\text{-}Al_2O_3$ (alloy) and $Rh+Pt/\gamma\text{-}Al_2O_3$ (mechanical mixture) catalysts. To study the effect of the surface hydroxylation under natural conditions, the $Pt/\gamma\text{-}Al_2O_3$ sample was additionally calcined in argon at 400 °C for 4 h immediately before the measurements. Such a low temperature of pretreatment was chosen to minimize any possible sintering effects. As known, the spectra of the Rh^{3+} (4d6) and Pt^{4+} (5d6) ions in the low-spin octahedral complexes are characterized by a charge transfer band and d-d transitions $^1A_{1g} \rightarrow {}^1T_{1g}$, $^1T_{2g}$. The representative value of the energy-gap width (E_g) of Rh^{3+} complexes for the $Rh/\gamma\text{-}Al_2O_3$ sample was equal to 2.49 eV (Figure 8, spectrum 2). Koffyberg has reported that the E_g value for Rh_2O_3 particles decreases from an asymptotic value of 2.59 eV for the isolated Rh^{3+} complexes to 1.2 eV for the bulk oxide Rh_2O_3 [107].

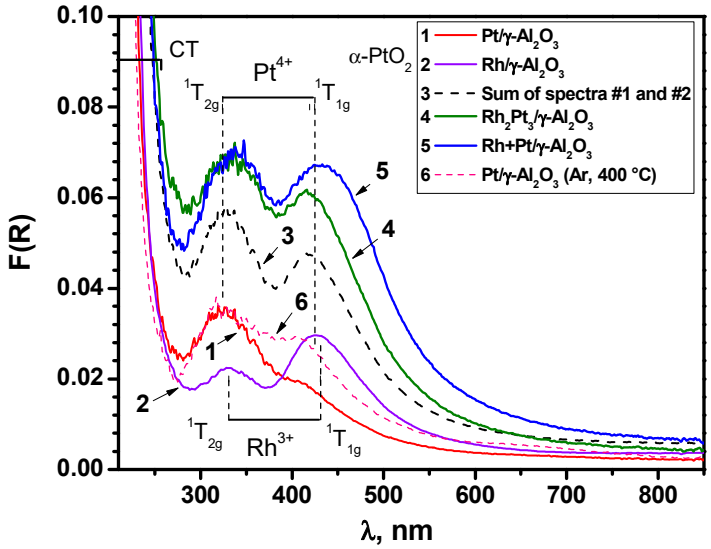

Figure 8. The diffuse reflectance UV-vis spectra of the samples Pt/γ-Al_2O_3, Rh/γ-Al_2O_3, Rh_2Pt_3/γ-Al_2O_3, and Rh+Pt/γ-Al_2O_3 treated at 400 °C, and sample Pt/γ-Al_2O_3 additionally calcined in argon at 400 °C. All the spectra are corrected concerning the support.

In the case of the Pt/γ-Al_2O_3 sample, the energy-gap width for Pt^{4+} complexes was about 2.62 eV. This value did not change noticeably after the dehydroxylation procedure in an argon flow at 400 °C, despite a slight increase in the intensity of the $^1A_{1g} \rightarrow {}^1T_{1g}$ band. Unfortunately, there is no information on the E_g value for the Pt^{4+} complexes in the literature. The experimental E_g values for the α-PtO_2 particles were varied in a range from 1.3 [108]ʹto 1.8 eV [109].

As evident from Figure 8, the sum of spectra 1 and 2 (Pt/γ-Al_2O_3 and Rh/γ-Al_2O_3 samples, accordingly) corresponded well to the spectra for the bimetallic samples Rh_2Pt_3/γ-Al_2O_3 and Rh+Pt/γ-Al_2O_3, despite the lower intensity. Such an approach was recently reported as efficient for the approximation of spectra of the bimetallic Rh_2Pd_3/γ-Al_2O_3 model catalysts [95]. Good agreement of the spectra for the binary systems with the spectra for the monometallic reference samples indicates that there were no significant distortions of the octahedral surrounding taking place during the formation of Rh_2Pd_3 oxide clusters. Long-wave edge of d-d transitions of the bimetallic samples at the present ratio of metals was mainly determined by Rh^{3+} ions. The values of the energy-gap width for the samples Rh_2Pt_3/γ-Al_2O_3 and Rh+Pt/γ-Al_2O_3 were equal to 2.47 and 2.34 eV, respectively. The sample Rh+Pt/γ-Al_2O_3 was characterized by a larger particle size in comparison with the sample Rh_2Pt_3/γ-Al_2O_3, which possessed practically the same E_g value as the reference sample Rh/γ-Al_2O_3.

Figure 9a shows the UV-vis spectra for the samples of the reference catalyst Pt/γ-Al_2O_3 treated at 400 °C (spectrum 2), aged under PTA conditions (spectrum 1), and treated in air at 400 °C for 6 h after aging under PTA conditions (spectrum 3). Left part of these spectra presented in Figure 9b demonstrates the charge transfer band for the same samples. Treatment in air was aimed to oxidize the reduced part of platinum and recover the initial hydroxyl coverage on the surface without any sintering effects. The observed appearance of an intensive band of the plasmon resonance in the UV region of the spectrum 1 testifies towards the formation of Pt^0 particles, while d-d transitions indicate the presence of oxidized Pt^{4+} species. The shift of the $^1A_{1g} \rightarrow {}^1T_{2g}$ band to the short-wave region can be assigned to the part exchange of the ligands in the Pt^{4+} complexes as a result of aging in the PTA regime, and to their interaction with metallic particles. The oxidative treatment of the catalyst in air leads to a decrease in intensity of the band in the UV region of the spectrum down to the initial level, thus indicating the oxidation of platinum. On the other hand, an increase in the intensity of d-d transitions of the Pt^{4+} complexes along with a shift of the absorption band's edge towards the long-wave region allows the conclusion about the formation of relatively large α–PtO_2 particles characterized by the E_g value of 1.65 eV.

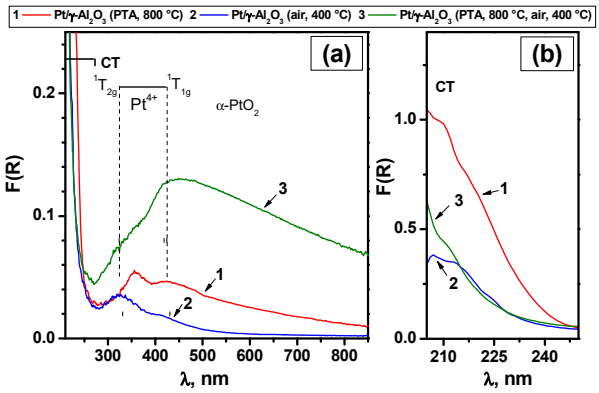

Figure 9. (**a**) The diffuse reflectance UV-vis spectra of samples Pt/γ-Al_2O_3 aged under PTA conditions, treated at 400 °C, and treated at 400 °C after aging under PTA conditions. All the spectra are corrected concerning the support. (**b**) The charge transfer part of the spectra.

The UV-vis spectra for the bimetallic catalysts Rh_2Pt_3/γ-Al_2O_3 and Rh+Pt/γ-Al_2O_3 and monometallic reference sample Pt/γ-Al_2O_3 after the prompt thermal aging experiments and subsequent treatment in air at 400 °C are shown in Figure 10. Corresponding values of the energy-gap width for the initial and aged samples are summarized in Table 6. It was evident that both the bimetallic samples were more thermally stable towards sintering if compared with the Pt/γ-Al_2O_3 reference, and possessed very close values of E_g 1.97–2.01 eV.

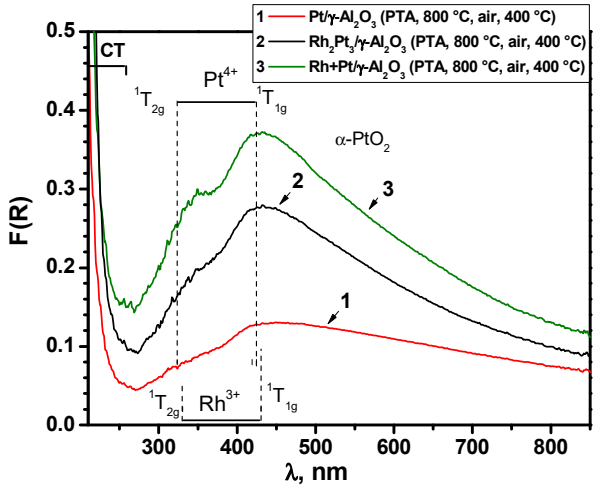

Figure 10. The diffuse reflectance UV-vis spectra of samples Pt/γ-Al_2O_3, Rh_2Pt_3/γ-Al_2O_3, and Rh+Pt/γ-Al_2O_3 aged at 800 °C and treated at 400 °C. All the spectra are corrected concerning the support.

Table 6. The values of the band gap (E_g) for the studied samples in the initial state and after aging under PTA conditions. All the samples were treated on air at 400 °C before the characterization.

Sample	E_g, eV	
	Initial	Aged at 800 °C
Pt/γ-Al_2O_3	2.62	1.65
Rh_2Pt_3/γ-Al_2O_3	2.47	1.97
Rh+Pt/γ-Al_2O_3	2.34	2.01
$Rh_2(Pd_{0.25}Pt_{0.75})_3$/γ-$Al_2O_3$	2.47	2.08
$Rh_2(Pd_{0.\ 5}Pt_{0.5})_3$/γ-$Al_2O_3$	2.44	2.17
$Rh_2(Pd_{0.75}Pt_{0.25})_3$/γ-$Al_2O_3$	2.43	2.30

The UV-vis spectra for the ternary systems $Rh_2(Pd_{0.25}Pt_{0.75})_3/\gamma\text{-}Al_2O_3$, $Rh_2(Pd_{0.5}Pt_{0.5})_3/\gamma\text{-}Al_2O_3$, and $Rh_2(Pd_{0.75}Pt_{0.25})_3/\gamma\text{-}Al_2O_3$ before and after the aging under PTA conditions are shown in Figure 11. In the initial state, the values of the energy-gap width for these catalysts were very close (Table 6). The sample $Rh_2(Pd_{0.25}Pt_{0.75})_3/\gamma\text{-}Al_2O_3$ containing the highest amount of platinum was characterized by a better dispersion of the alloy nanoparticles (Figure 11a). The aging of the samples at 800 °C changed significantly the situation. In this case, the samples could be ranked by a decreased dispersion as $Rh_2(Pd_{0.75}Pt_{0.25})_3/\gamma\text{-}Al_2O_3 > Rh_2(Pd_{0.5}Pt_{0.5})_3/\gamma\text{-}Al_2O_3 > Rh_2(Pd_{0.25}Pt_{0.75})_3/\gamma\text{-}Al_2O_3$. The E_g values for the samples $Rh_2(Pd_{0.75}Pt_{0.25})_3/\gamma\text{-}Al_2O_3$ and $Rh_2(Pd_{0.5}Pt_{0.5})_3/\gamma\text{-}Al_2O_3$ were 2.3 and 2.17 eV, accordingly. Thereby, in terms of dispersion of the active component, the ternary alloy systems surpassed the bimetallic and monometallic catalysts.

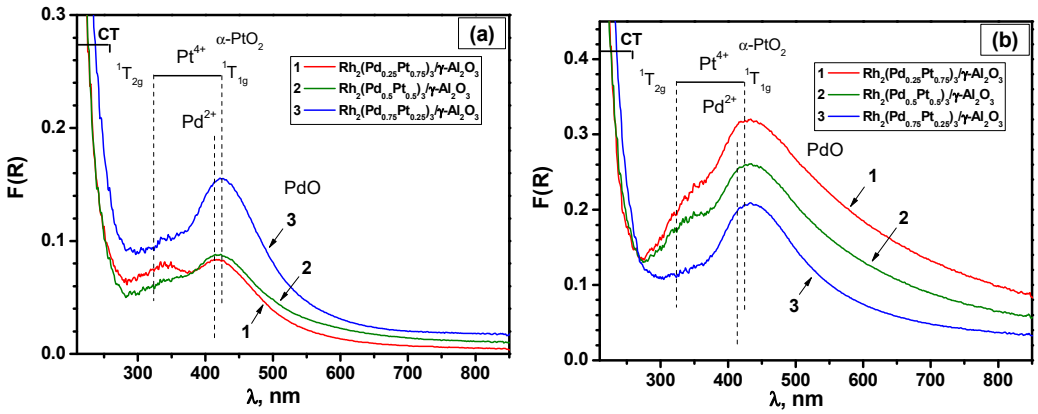

Figure 11. The diffuse reflectance UV-vis spectra of samples $Rh_2(Pd_{0.25}Pt_{0.75})_3/\gamma\text{-}Al_2O_3$, $Rh_2(Pd_{0.5}Pt_{0.5})_3/\gamma\text{-}Al_2O_3$, and $Rh_2(Pd_{0.75}Pt_{0.25})_3/\gamma\text{-}Al_2O_3$ treated at 400 °C: (**a**) initial and (**b**) aged at 800 °C under PTA conditions. All the spectra are corrected concerning the support.

It was already mentioned that the Pt-only catalyst underwent noticeable reactivation after the aging at 800 °C. Its catalytic activity in the 6th and 7th runs was comparable with that for the binary and ternary catalysts (Figure 7). On the other hand, as it follows from the UV-vis spectroscopy data (Figure 9a), the active Pt species after the PTA aging were predominantly represented by the Pt^{4+} complexes. For the ternary systems, the higher amount of these forms is observed in the case of $Rh_2(Pd_{0.5}Pt_{0.5})_3/\gamma\text{-}Al_2O_3$ (Figure 11, spectrum 2). Possibly, this explains the better catalytic performance (high initial activity and appropriate stability) of this sample.

Summarizing all the data presented above, it should be mentioned that the concept of a single-source precursor is applicable and quite efficient for the preparation of the supported ternary Rh-Pd-Pt catalysts. The thermolysis of the solid solutions of the double complex salts used as such precursors allows for obtaining of the ternary alloys with a predefined metal ratio. Thus, the final catalytic properties of the catalysts can be easily tuned.

4. Conclusions

Precious metals supported on different supports (alumina, ceria, and zirconia) are widely attractive due to their excellent catalytic properties in various industrially and environmentally important processes. For instance, one of the areas of their application is three-way catalysis aimed to reduce the emissions from gasoline engines. The requirements imposed for such catalytic converters are an appropriate activity in the catalyzed reactions (oxidation of CO and hydrocarbons, and reduction of nitrogen oxides) and long-term stability including the resistance towards the elevated temperatures. The CO oxidation reaction is commonly used as a model reaction for screening the prospective catalytic compositions. The present work is purposed in studying the applicability of a single-source precursor concept to prepare the ternary nanoalloys with improved catalytic characteristics. A series of the catalysts were prepared by an incipient wetness impregnation of the alumina support with an aqueous

solution of the corresponding complex salt containing one, two, or three metals (Rh, Pd, and Pt). The formation of alloys as a result of the precursor's thermolysis in a reductive medium was confirmed by the XRD and TEM methods. The phase diagram for the ternary Rh-Pd-Pt system at temperatures 600, 700, and 800 °C was proposed for the first time. The prepared samples were examined in the CO oxidation reaction performed under prompt thermal aging conditions. It was shown that the introduction of palladium into the composition of the active particles improves the initial activity along with appropriate stability at high temperatures. The best catalytic performance was exhibited by the $Rh_2(Pd_{0.5}Pt_{0.5})_3/\gamma$-$Al_2O_3$ sample with equal amounts of platinum and palladium. The characterization of the catalysts by a diffuse reflectance UV-vis spectroscopy has revealed that palladium affects the dispersion of the nanoparticles: the higher the amount of Pd that is introduced, the better dispersion is. The extraordinary activity of the $Rh_2(Pd_{0.5}Pt_{0.5})_3/\gamma$-$Al_2O_3$ sample is assigned to the presence of Pt in the form of the Pt^{4+} complexes.

Author Contributions: Conceptualization, A.A.V. and Y.V.S.; methodology, A.A.V. and Y.V.S.; investigation, R.M.K., P.E.P. and V.O.S.; writing—original draft preparation, A.A.V., Y.V.S. and P.E.P.; writing—review and editing, A.A.V.; project administration, Y.V.S.; funding acquisition, Y.V.S. All authors have read and agreed to the published version of the manuscript.

Funding: This research was funded by the Russian Science Foundation, grant number 16-13-10192.

Acknowledgments: Characterization of the samples was performed using the equipment of the Center of Collective Use "National Center of Catalysts Research".

Conflicts of Interest: The funders had no role in the design of the study; in the collection, analyses, or interpretation of data; in the writing of the manuscript, or in the decision to publish the results.

References

1. Cheng, D.; Xu, H.; Fortunelli, A. Tuning the catalytic activity of Au–Pd nanoalloys in CO oxidation via composition. *J. Catal.* **2014**, *314*, 47–55. [CrossRef]
2. Kang, N.; Ng, M.S.; Shan, S.; Wu, J.; Zhao, W.; Yin, J.; Fang, W.; Luo, J.; Petkov, V.; Zhong, C.-J. Synergistic catalytic properties of bifunctional nanoalloy catalysts in rechargeable lithium-oxygen battery. *J. Power Sources* **2016**, *326*, 60–69. [CrossRef]
3. Ruiz-Ruiz, V.-F.; González-Olvera, R.; Díaz-Pardo, R.; Betancourt, I.; Zumeta-Dubé, I.; Díaz, D.; Farfán, N.; Arellano-Jiménez, M.J. Mechanochemically obtained Pd–Ag nanoalloys. Structural considerations and catalytic activity. *Materialia* **2018**, *4*, 166–174. [CrossRef]
4. Zhang, Y.; Gao, F.; Fu, M.-L. Composite of Au-Pd nanoalloys/reduced graphene oxide toward catalytic selective organic transformation to fine chemicals. *Chem. Phys. Lett.* **2018**, *691*, 61–67. [CrossRef]
5. Taran, S. Composition effect on melting behaviors of Cu-Au-Pt trimetallic nanoalloys. *Comput. Theor. Chem.* **2019**, *1166*, 112576. [CrossRef]
6. Campos-Roldán, C.A.; Calvillo, L.; Granozzi, G.; Alonso-Vante, N. Alkaline hydrogen electrode and oxygen reduction reaction on PtxNi nanoalloys. *J. Electroanal. Chem.* **2020**, *857*, 113449. [CrossRef]
7. Liu, X.; Wu, J.; Guo, X. Ternary boron-, phosphorus- and oxygen-doped amorphous nickel nanoalloys for enhanced activity towards the oxygen evolution reaction. *Electrochem. Commun.* **2020**, *111*, 106649. [CrossRef]
8. Cizmeci, M.; Musavi, A.; Tekin, A.; Kayahan, M. Comparison of two palladium catalysts on different supports during hydrogenation. *J. Am. Oil Chem. Soc.* **2006**, *83*, 1063–1068. [CrossRef]
9. Vishwanathan, V.; Jayasri, V.; Mahaboob Basha, P. Vapor phase hydrogenation of o-chloronitrobenzene (o-CNB) over alumina supported palladium catalyst—A kinetic study. *Reac. Kinet. Catal. Lett.* **2007**, *91*, 291–298. [CrossRef]
10. Fukuyama, T.; Kippo, T.; Ryu, I.; Sagae, T. Addition of allyl bromide to phenylacetylene catalyzed by palladium on alumina and its application to a continuous flow synthesis. *Res. Chem. Intermediat.* **2009**, *35*, 1053–1057. [CrossRef]
11. Arora, S.; Kapoor, P.; Singla, M.L. Catalytic studies of palladium nanoparticles immobilized on alumina synthesized by a simple physical precipitation method. *Reac. Kinet. Mech. Catal.* **2010**, *99*, 157–165. [CrossRef]
12. Hong, U.G.; Hwang, S.; Seo, J.G.; Yi, J.; Song, I.K. Hydrogenation of Succinic Acid to γ-Butyrolactone over Palladium Catalyst Supported on Mesoporous Alumina Xerogel. *Catal. Lett.* **2010**, *138*, 28–33. [CrossRef]

13. Berenblyum, A.S.; Podoplelova, T.A.; Shamsiev, R.S.; Katsman, E.A.; Danyushevsky, V.Y. On the mechanism of catalytic conversion of fatty acids into hydrocarbons in the presence of palladium catalysts on alumina. *Petroleum Chem.* **2011**, *51*, 336–341. [CrossRef]
14. Thomazeau, C.; Cseri, T.; Bisson, L.; Aguilhon, J.; Pham Minh, D.; Boissière, C.; Durupthy, O.; Sanchez, C. Nano Design of Alumina Supported Monometallic Catalysts: A Promising Way to Improve the Selective Hydrogenation of Poly-Unsaturated Hydrocarbons. *Top. Catal.* **2012**, *55*, 690–699. [CrossRef]
15. Chen, L.; Feng, T.; Wang, P.; Xiang, Y.; Ou, B. Catalytic properties of Pd supported on hexaaluminate coated alumina in low temperature combustion of coal mine ventilation air methane. *Kinet. Catal.* **2013**, *54*, 767–772. [CrossRef]
16. Voskanyan, P.S. Effect of the nature of a support on the catalytic activity of a palladium catalyst in the synthesis of vinyl acetate by gas-phase ethylene acetoxylation. *Catal. Ind.* **2013**, *5*, 90–97. [CrossRef]
17. Weng, X.; Yuan, X.; Li, H.; Li, X.; Chen, M.; Wan, H. The study of the active surface for CO oxidation over supported Pd catalysts. *Sci. China Chem.* **2014**, *58*, 174–179. [CrossRef]
18. Ravanchi, M.T.; Fadaeerayeni, S.; Fard, M.R. The effect of calcination temperature on physicochemical properties of alumina as a support for acetylene selective hydrogenation catalyst. *Res. Chem. Intermediat.* **2015**, *42*, 4797–4811. [CrossRef]
19. Glyzdova, D.V.; Vedyagin, A.A.; Tsapina, A.M.; Kaichev, V.V.; Trigub, A.L.; Trenikhin, M.V.; Shlyapin, D.A.; Tsyrulnikov, P.G.; Lavrenov, A.V. A study on structural features of bimetallic Pd-M/C (M: Zn, Ga, Ag) catalysts for liquid-phase selective hydrogenation of acetylene. *Appl. Catal. A-Gen.* **2018**, *563*, 18–27. [CrossRef]
20. Iost, K.N.; Borisov, V.A.; Temerev, V.L.; Surovikin, Y.V.; Pavluchenko, P.E.; Trenikhin, M.V.; Arbuzov, A.B.; Shlyapin, D.A.; Tsyrulnikov, P.G.; Vedyagin, A.A. Carbon support hydrogenation in Pd/C catalysts during reductive thermal treatment. *Int. J. Hydrog. Energ.* **2018**, *43*, 17656–17663. [CrossRef]
21. Glyzdova, D.V.; Khramov, E.V.; Smirnova, N.S.; Prosvirin, I.P.; Bukhtiyarov, A.V.; Trenikhin, M.V.; Gulyaeva, T.I.; Vedyagin, A.A.; Shlyapin, D.A.; Lavrenov, A.V. Study on the active phase formation of Pd-Zn/Sibunit catalysts during the thermal treatment in hydrogen. *Appl. Surf. Sci.* **2019**, *483*, 730–741. [CrossRef]
22. Monteiro, R.S.; Dieguez, L.C.; Schmal, M. The role of Pd precursors in the oxidation of carbon monoxide over Pd/Al_2O_3 and $Pd/CeO_2/Al_2O_3$ catalysts. *Catal. Today* **2001**, *65*, 77–89. [CrossRef]
23. Demoulin, O.; Navez, M.; Ruiz, P. The Activation of a Pd/γ-alumina Catalyst During Methane Combustion: Investigation of the Phenomenon and of Potential Causes. *Catal. Lett.* **2005**, *103*, 149–153. [CrossRef]
24. Gopinath, R.; Babu, N.S.; Kumar, J.V.; Lingaiah, N.; Prasad, P.S. Influence of Pd Precursor and Method of Preparation on Hydrodechlorination Activity of Alumina Supported Palladium Catalysts. *Catal. Lett.* **2007**, *120*, 312–319. [CrossRef]
25. Li, G.; Wang, Q.; Zhao, B.; Zhou, R. A new insight into the role of transition metals doping with CeO_2–ZrO_2 and its application in Pd-only three-way catalysts for automotive emission control. *Fuel* **2012**, *92*, 360–368. [CrossRef]
26. Zhou, Y.; Wang, Z.; Liu, C. Perspective on CO oxidation over Pd-based catalysts. *Catal. Sci. Technol.* **2015**, *5*, 69–81. [CrossRef]
27. Vedyagin, A.; Volodin, A.; Kenzhin, R.; Chesnokov, V.; Mishakov, I. CO Oxidation over Pd/ZrO2 Catalysts: Role of Support's Donor Sites. *Molecules* **2016**, *21*, 1289. [CrossRef]
28. Vedyagin, A.A.; Volodin, A.M.; Kenzhin, R.M.; Stoyanovskii, V.O.; Rogov, V.A.; Kriventsov, V.V.; Mishakov, I.V. The role of chemisorbed water in formation and stabilization of active sites on Pd/Alumina oxidation catalysts. *Catal. Today* **2018**, *307*, 102–110. [CrossRef]
29. Ferri, D.; Elsener, M.; Kröcher, O. Methane oxidation over a honeycomb Pd-only three-way catalyst under static and periodic operation. *Appl. Catal. B-Environ.* **2018**, *220*, 67–77. [CrossRef]
30. Yu, W.; Porosoff, M.D.; Chen, J.G. Review of Pt-Based Bimetallic Catalysis: From Model Surfaces to Supported Catalysts. *Chem. Rev.* **2012**, *112*, 5780–5817. [CrossRef]
31. Kogan, S.B.; Herskowitz, M. Geometric and electronic factors in paraffin dehydrogenation on bimetallic platinum catalysts. *Reac. Kinet. Catal. Lett.* **2005**, *85*, 341–345. [CrossRef]
32. Antolini, E. Formation, microstructural characteristics and stability of carbon supported platinum catalysts for low temperature fuel cells. *J. Mater. Sci.* **2003**, *38*, 2995–3005. [CrossRef]
33. Seselj, N.; Engelbrekt, C.; Zhang, J. Graphene-supported platinum catalysts for fuel cells. *Sci. Bull.* **2015**, *60*, 864–876. [CrossRef]

34. Fuente, A.M.; Pulgar, G.; González, F.; Pesquera, C.; Blanco, C. Activated carbon supported Pt catalysts: Effect of support texture and metal precursor on activity of acetone hydrogenation. *Appl. Catal. A-Gen.* **2001**, *208*, 35–46. [CrossRef]
35. Román-Martínez, M.C.; Cazorla-Amorós, D.; Linares-Solano, A.; de Lecea, C.S.-M. Carbon dioxide hydrogenation catalyzed by alkaline earth- and platinum-based catalysts supported on carbon. *Appl. Catal. A-Gen.* **1994**, *116*, 187–204. [CrossRef]
36. Du, J.-P.; Song, C.; Song, J.-L.; Zhao, J.-H.; Zhu, Z.-P. Cyclohexane dehydrogenation over the platinum catalysts supported on carbon nanomaterials. *J. Fuel Chem. Technol.* **2009**, *37*, 468–472. [CrossRef]
37. Arevalo-Bastante, A.; Álvarez-Montero, M.A.; Bedia, J.; Gómez-Sainero, L.M.; Rodriguez, J.J. Gas-phase hydrodechlorination of mixtures of chloromethanes with activated carbon-supported platinum catalysts. *Appl. Catal. B-Environ.* **2015**, *179*, 551–557. [CrossRef]
38. Auer, E.; Freund, A.; Pietsch, J.; Tacke, T. Carbons as supports for industrial precious metal catalysts. *Appl. Catal. A-Gen.* **1998**, *173*, 259–271. [CrossRef]
39. Shelef, M.; Graham, G.W. Why Rhodium in Automotive Three-Way Catalysts? *Catal. Rev.* **2006**, *36*, 433–457. [CrossRef]
40. Trzeciak, A.M.; Ziółkowski, J.J.; Jaworska-Galas, Z.; Migta, W.; Wrzyszcz, J. Homogeneous and alumina supported rhodium complex catalysed hydrogenation. *J. Mol. Catal.* **1994**, *88*, 13–21. [CrossRef]
41. Alini, S.; Bottino, A.; Capannelli, G.; Carbone, R.; Comite, A.; Vitulli, G. The catalytic hydrogenation of adiponitrile to hexamethylenediamine over a rhodium/alumina catalyst in a three phase slurry reactor. *J. Mol. Catal. A-Chem.* **2003**, *206*, 363–370. [CrossRef]
42. Hebben, N.; Diehm, C.; Deutschmann, O. Catalytic partial oxidation of ethanol on alumina-supported rhodium catalysts: An experimental study. *Appl. Catal. A-Gen.* **2010**, *388*, 225–231. [CrossRef]
43. Hung, C.M. Characterization and performance of Pt-Pd-Rh cordierite monolith catalyst for selectivity catalytic oxidation of ammonia. *J. Hazard. Mater.* **2010**, *180*, 561–565. [CrossRef] [PubMed]
44. Zapf, R.; Thiele, R.; Wichert, M.; O'Connell, M.; Ziogas, A.; Kolb, G. Application of rhodium nanoparticles for steam reforming of propane in microchannels. *Catal. Commun.* **2013**, *41*, 140–145. [CrossRef]
45. Choi, K.; Joo, J.M.; Lee, C. Rhodium-catalyzed tandem addition–cyclization of alkynylimines. *Tetrahedron* **2015**, *71*, 5910–5917. [CrossRef]
46. Zhang, Q.; Mixdorf, J.C.; Reynders, G.J.; Nguyen, H.M. Rhodium-catalyzed benzylic fluorination of trichloroacetimidates. *Tetrahedron* **2015**, *71*, 5932–5938. [CrossRef]
47. Özhava, D.; Özkar, S. Nanoalumina-supported rhodium(0) nanoparticles as catalyst in hydrogen generation from the methanolysis of ammonia borane. *Mol. Catal.* **2017**, *439*, 50–59. [CrossRef]
48. Kiss, B.; Manning, T.D.; Hesp, D.; Didier, C.; Taylor, A.; Pickup, D.M.; Chadwick, A.V.; Allison, H.E.; Dhanak, V.R.; Claridge, J.B.; et al. Nano-structured rhodium doped SrTiO3–Visible light activated photocatalyst for water decontamination. *Appl. Catal. B-Environ.* **2017**, *206*, 547–555. [CrossRef]
49. Coq, B.; Figueras, F. Bimetallic palladium catalysts: Influence of the co-metal on the catalyst performance. *J. Mol. Catal. A-Chem.* **2001**, *173*, 117–134. [CrossRef]
50. Hungría, A.B.; Iglesias-Juez, A.; Martínez-Arias, A.; Fernández-García, M.; Anderson, J.A.; Conesa, J.C.; Soria, J. Effects of Copper on the Catalytic Properties of Bimetallic Pd–Cu/(Ce,Zr)Ox/Al2O3 and Pd–Cu/(Ce,Zr)Ox Catalysts for CO and NO Elimination. *J. Catal.* **2002**, *206*, 281–294. [CrossRef]
51. Fernández-García, M.; Martínez-Arias, A.; Iglesias-Juez, A.; Hungría, A.B.; Anderson, J.A.; Conesa, J.C.; Soria, J. Behavior of bimetallic Pd-Cr/Al2O3 and Pd-Cr/(Ce,Zr)Ox/Al2O3 catalysts for CO and NO elimination. *J. Catal.* **2003**, *214*, 220–233. [CrossRef]
52. Ershov, B.G.; Anan'ev, A.V.; Abkhalimov, E.V.; Kochubei, D.I.; Kriventsov, V.V.; Plyasova, L.M.; Molina, I.Y.; Kozitsyna, N.Y.; Nefedov, S.E.; Vargaftik, M.N.; et al. Bimetallic Pd-M (M = Co, Ni, Zn, Ag) nanoparticles containing transition metals: Synthesis, characterization, and catalytic performance. *Nanotechnol. Russ.* **2011**, *6*, 323–329. [CrossRef]
53. Hinokuma, S.; Katsuhara, Y.; Ando, E.; Ikeue, K.; Machida, M. PdFe/CeO_2 bimetal catalysts prepared by dual arc-plasma deposition. *Catal. Today* **2013**, *201*, 92–97. [CrossRef]
54. Hilli, Y.; Kinnunen, N.M.; Suvanto, M.; Savimäki, A.; Kallinen, K.; Pakkanen, T.A. Preparation and characterization of Pd–Ni bimetallic catalysts for CO and C3H6 oxidation under stoichiometric conditions. *Appl. Catal. A-Gen.* **2015**, *497*, 85–95. [CrossRef]

55. Shan, S.; Petkov, V.; Prasai, B.; Wu, J.; Joseph, P.; Skeete, Z.; Kim, E.; Mott, D.; Malis, O.; Luo, J.; et al. Catalytic activity of bimetallic catalysts highly sensitive to the atomic composition and phase structure at the nanoscale. *Nanoscale* **2015**, *7*, 18936–18948. [CrossRef] [PubMed]
56. Xu, Z.F.; Wang, Y.X. Effects of Alloyed Metal on the Catalysis Activity of Pt for Ethanol Partial Oxidation: Adsorption and Dehydrogenation on Pt3M (M = Pt, Ru, Sn, Re, Rh, and Pd). *J. Phys. Chem. C* **2011**, *115*, 20565–20571. [CrossRef]
57. Shubin, Y.V.; Vedyagin, A.A.; Plyusnin, P.E.; Kirilovich, A.K.; Kenzhin, R.M.; Stoyanovskii, V.O.; Korenev, S.V. The peculiarities of Au–Pt alloy nanoparticles formation during the decomposition of double complex salts. *J. Alloys Compnd.* **2018**, *740*, 935–940. [CrossRef]
58. Nunan, J.G.; Williamson, W.B.; Robota, H.J.; Henk, M.G. Impact of Pt-Rh and Pd-Rh Interactions on Performance of Bimetal Catalysts. *SAE Tech. Paper* **1995**, 950258. [CrossRef]
59. Araya, P.; Díaz, V. Synergism in the reaction of CO with O_2 on bimetallic Rh-Pd catalysts supported on silica. *J. Chem. Soc. Faraday Trans.* **1997**, *93*, 3887–3891. [CrossRef]
60. Wu, X.; Xu, L.; Weng, D. The thermal stability and catalytic performance of Ce-Zr promoted Rh-Pd/γ-Al2O3 automotive catalysts. *Appl. Surf. Sci.* **2004**, *221*, 375–383. [CrossRef]
61. De Sarkar, A.; Khanra, B. CO oxidation and NO reduction over supported Pt-Rh and Pd-Rh nanocatalysts: A comparative study. *J. Mol. Catal. A-Chem.* **2005**, *229*, 25–29. [CrossRef]
62. Hangas, J.; Chen, A.E. Comparative Analytical Study of Two Pt–Rh Three-way Catalysts. *Catal. Lett.* **2006**, *108*, 103–111. [CrossRef]
63. Renzas, J.R.; Huang, W.; Zhang, Y.; Grass, M.E.; Somorjai, G.A. Rh1−xPdx Nanoparticle Composition Dependence in CO Oxidation by NO. *Catal. Lett.* **2010**, *141*, 235–241. [CrossRef]
64. Büchel, R.; Pratsinis, S.E.; Baiker, A. Mono-and bimetallic Rh and Pt NSR-catalysts prepared by controlled deposition of noble metals on support or storage component. *Appl. Catal. B-Environ.* **2012**, *113–114*, 160–171. [CrossRef]
65. Vedyagin, A.A.; Volodin, A.M.; Stoyanovskii, V.O.; Kenzhin, R.M.; Slavinskaya, E.M.; Mishakov, I.V.; Plyusnin, P.E.; Shubin, Y.V. Stabilization of active sites in alloyed Pd–Rh catalysts on γ-Al2O3 support. *Catal. Today* **2014**, *238*, 80–86. [CrossRef]
66. Zhan, Z.; Song, L.; Liu, X.; Jiao, J.; Li, J.; He, H. Effects of synthesis methods on the performance of Pt + Rh/Ce0.6Zr0.4O_2 three-way catalysts. *J. Environ. Sci.* **2014**, *26*, 683–693. [CrossRef]
67. Shang, H.; Wang, Y.; Cui, Y.; Fang, R.; Hu, W.; Gong, M.; Chen, Y. Catalytic performance of Pt–Rh/CeZrYLa+LaAl with stoichiometric natural gas vehicles emissions. *Chinese J. Catal.* **2015**, *36*, 290–298. [CrossRef]
68. Vedyagin, A.A.; Plyusnin, P.E.; Rybinskaya, A.A.; Shubin, Y.V.; Mishakov, I.V.; Korenev, S.V. Synthesis and study of Pd-Rh alloy nanoparticles and alumina-supported low-content Pd-Rh catalysts for CO oxidation. *Mater. Res. Bull.* **2018**, *102*, 196–202. [CrossRef]
69. Shubin, Y.V.; Plyusnin, P.E.; Korenev, S.V. Determination of the equilibrium miscibility gap in the Pd–Rh alloy system using metal nanopowders obtained by decomposition of coordination compounds. *J. Alloys Compnd.* **2015**, *622*, 1055–1060. [CrossRef]
70. Vedyagin, A.A.; Stoyanovskii, V.O.; Plyusnin, P.E.; Shubin, Y.V.; Slavinskaya, E.M.; Mishakov, I.V. Effect of metal ratio in alumina-supported Pd-Rh nanoalloys on its performance in three way catalysis. *J. Alloys Compnd.* **2018**, *749*, 155–162. [CrossRef]
71. Kostin, G.A.; Plyusnin, P.E.; Filatov, E.Y.; Kuratieva, N.V.; Vedyagin, A.A.; Kal'nyi, D.B. Double complex salts [PdL4][RuNO(NO_2)$_4$OH] (L = NH_3, Py) synthesis, structure and preparation of bimetallic metastable solid solution Pd0.5Ru0.5. *Polyhedron* **2019**, *159*, 217–225. [CrossRef]
72. Sakamoto, Y.; Ohira, K.; Kokubu, M.; Flanagan, T.B. Thermodynamic properties for solution of hydrogen in Pd-Pt-Rh ternary alloys. *J. Alloys Compnd.* **1997**, *253*, 212–215. [CrossRef]
73. Lukaszewski, M.; Grden, M.; Czerwinski, A. Cyclic voltammetric behavior of Pd-Pt-Rh ternary alloys. *J. Solid State Electr.* **2005**, *9*, 1–9. [CrossRef]
74. Chen, Y.; Liao, S.Z.; Deng, H.Q. The Rh influence on the surface distribution of the ternary alloy Pt-Pd-Rh. *Appl. Surf. Sci.* **2007**, *253*, 6074–6079. [CrossRef]
75. Luyten, J.; Creemers, C. Surface segregation in ternary Pt-Pd-Rh alloys studied with Monte Carlo simulations and the modified embedded atom method. *Surf. Sci.* **2008**, *602*, 2491–2495. [CrossRef]

76. Bhagiyalakshmi, M.; Anuradha, R.; Park, S.D.; Park, T.S.; Cha, W.S.; Jang, H.T. Effect of Bimetallic Pt-Rh and Trimetallic Pt-Pd-Rh Catalysts for Low Temperature Catalytic Combustion of Methane. *B. Korean Chem. Soc.* **2010**, *31*, 120–124. [CrossRef]
77. Hung, C.M. Cordierite-supported Pt-Pd-Rh ternary composite for selective catalytic oxidation of ammonia. *Powder Technol.* **2010**, *200*, 78–83. [CrossRef]
78. Bagot, P.A.J.; Kruska, K.; Haley, D.; Carrier, X.; Marceau, E.; Moody, M.P.; Smith, G.D.W. Oxidation and Surface Segregation Behavior of a Pt-Pd-Rh Alloy Catalyst. *J. Phys. Chem. C* **2014**, *118*, 26130–26138. [CrossRef]
79. Sarker, M.S.I.; Nakamura, T.; Sato, S. Composition-controlled ternary Rh-Pd-Pt solid-solution alloy nanoparticles by laser irradiation of mixed solution of metallic ions. *J. Mater. Res.* **2014**, *29*, 856–864. [CrossRef]
80. Liu, T.D.; Xu, L.Y.; Shao, G.F.; Tu, N.N.; Tao, J.P.; Wen, Y.H. Structural optimization of Pt-Pd-Rh trimetallic nanoparticles using improved genetic algorithm. *J. Alloys Compnd.* **2016**, *663*, 466–473. [CrossRef]
81. Liu, X.; Han, Y.Q.; Jia, H.S. Pt-Rh-Pd Alloy Group Gauze Catalysts Used for Ammonia Oxidation. *Rare Met. Mater. Eng.* **2017**, *46*, 339–343.
82. Vedyagin, A.A.; Volodin, A.M.; Stoyanovskii, V.O.; Mishakov, I.V.; Medvedev, D.A.; Noskov, A.S. Characterization of active sites of Pd/Al2O3 model catalysts with low Pd content by luminescence, EPR and ethane hydrogenolysis. *Appl. Catal. B-Environ.* **2011**, *103*, 397–403. [CrossRef]
83. Stoyanovskii, V.O.; Vedyagin, A.A.; Aleshina, G.I.; Volodin, A.M.; Noskov, A.S. Characterization of Rh/Al2O3 catalysts after calcination at high temperatures under oxidizing conditions by luminescence spectroscopy and catalytic hydrogenolysis. *Appl. Catal. B-Environ.* **2009**, *90*, 141–146. [CrossRef]
84. Chen, X.; Cheng, Y.; Seo, C.Y.; Schwank, J.W.; McCabe, R.W. Aging, re-dispersion, and catalytic oxidation characteristics of model Pd/Al2O3 automotive three-way catalysts. *Appl. Catal. B-Environ.* **2015**, *163*, 499–509. [CrossRef]
85. Morgan, K.; Goguet, A.; Hardacre, C. Metal Redispersion Strategies for Recycling of Supported Metal Catalysts: A Perspective. *Acs Catal.* **2015**, *5*, 3430–3445. [CrossRef]
86. Lupescu, J.A.; Schwank, J.W.; Fisher, G.B.; Chen, X.; Peczonczyk, S.L.; Drews, A.R. Pd model catalysts: Effect of aging duration on lean redispersion. *Appl. Catal. B-Environ.* **2016**, *185*, 189–202. [CrossRef]
87. Lupescu, J.A.; Schwank, J.W.; Fisher, G.B.; Hangas, J.; Peczonczyk, S.L.; Paxton, W.A. Pd model catalysts: Effect of air pulse length during redox aging on Pd redispersion. *Appl. Catal. B-Environ.* **2018**, *223*, 76–90. [CrossRef]
88. Seo, C.Y.; Chen, X.Y.; Sun, K.; Allard, L.F.; Fisher, G.B.; Schwank, J.W. Palladium redispersion at high temperature within the Pd@SiO2 core@shell structure. *Catal. Commun.* **2018**, *108*, 73–76. [CrossRef]
89. Fernandes, D.M.; Scofield, C.F.; Neto, A.A.; Cardoso, M.J.B.; Zotin, F.M.Z. Thermal deactivation of Pt/Rh commercial automotive catalysts. *Chem. Eng. J.* **2010**, *160*, 85–92. [CrossRef]
90. Vedyagin, A.A.; Stoyanovskii, V.O.; Kenzhin, R.M.; Slavinskaya, E.M.; Plyusnin, P.E.; Shubin, Y.V. Purification of gasoline exhaust gases using bimetallic Pd–Rh/δ-Al2O3 catalysts. *Reac. Kinet. Mech. Catal.* **2019**, *127*, 137–148. [CrossRef]
91. Kraus, W.; Nolze, G. POWDER CELL—A program for the representation and manipulation of crystal structures and calculation of the resulting X-ray powder patterns. *J. Appl. Crystallogr.* **1996**, *29*, 301–303. [CrossRef]
92. Krumm, S. An Interactive Windows Program for Profile Fitting and Size/Strain Analysis. *Mater. Sci. Forum* **1996**, *228*, 183–190. [CrossRef]
93. Stoyanovskii, V.O.; Vedyagin, A.A.; Volodin, A.M.; Kenzhin, R.M.; Slavinskaya, E.M.; Plyusnin, P.E.; Shubin, Y.V. Optical Spectroscopy Methods in the Estimation of the Thermal Stability of Bimetallic Pd–Rh/Al2O3 Three-Way Catalysts. *Top. Catal.* **2018**, *62*, 296–304. [CrossRef]
94. Vedyagin, A.A.; Gavrilov, M.S.; Volodin, A.M.; Stoyanovskii, V.O.; Slavinskaya, E.M.; Mishakov, I.V.; Shubin, Y.V. Catalytic Purification of Exhaust Gases Over Pd–Rh Alloy Catalysts. *Top. Catal.* **2013**, *56*, 1008–1014. [CrossRef]
95. Vedyagin, A.A.; Volodin, A.M.; Kenzhin, R.M.; Stoyanovskii, V.O.; Shubin, Y.V.; Plyusnin, P.E.; Mishakov, I.V. Effect of metal-metal and metal-support interaction on activity and stability of Pd-Rh/alumina in CO oxidation. *Catal. Today* **2017**, *293-294*, 73–81. [CrossRef]

96. Vedyagin, A.A.; Shubin, Y.V.; Kenzhin, R.M.; Plyusnin, P.E.; Stoyanovskii, V.O.; Volodin, A.M. Prospect of Using Nanoalloys of Partly Miscible Rhodium and Palladium in Three-Way Catalysis. *Top. Catal.* **2018**, *62*, 305–314. [CrossRef]
97. Pd-Pt Binary Phase Diagram 0-100, at. *Pd-Pt Binary Phase Diagram 0-100 at.% Pt: Datasheet from "PAULING FILE Multinaries Edition—2012" in SpringerMaterials*; Villars2016:sm_isp_c_0979992; Springer: Berlin/Heidelberg, Germany; Material Phases Data System (MPDS): Vitznau, Switzerland; National Institute for Materials Science (NIMS): Tsukuba, Japan.
98. Pt-Rh Binary Phase Diagram 0-100, at. *Pt-Rh Binary Phase Diagram 0-100 at.% Rh: Datasheet from "PAULING FILE Multinaries Edition—2012" in SpringerMaterials*; Villars2016:sm_isp_c_0979899; Springer: Berlin/Heidelberg, Germany; Material Phases Data System (MPDS): Vitznau, Switzerland; National Institute for Materials Science (NIMS): Tsukuba, Japan.
99. Bharadwaj, S.R.; Tripathi, S.N. The Pd-Pt (palladium-platinum) system. *J. Alloy Phase Diagr.* **1990**, *6*, 118–121.
100. Bharadwaj, S.R.; Kerkar, A.S.; Tripathi, S.N.; Dharwadkar, S.R. The palladium-platinum phase diagram. *J. Less Common Met.* **1991**, *169*, 167–172. [CrossRef]
101. Shubin, Y.V.; Korenev, S.V.; Sharafutdinov, M.R. High-temperature X-ray diffraction study of thermolysis of the double complex salt $[Rh(NH_3)_5Cl][PtCl_4]$. *Russ. Chem. Bull.* **2006**, *55*, 1109–1113. [CrossRef]
102. Zhao, J.C.; Jackson, M.R.; Peluso, L.A.; Brewer, L.N. A diffusion-multiple approach for mapping phase diagrams, hardness, and elastic modulus. *JOM* **2002**, *54*, 42–45. [CrossRef]
103. Zhao, J.C. Reliability of the diffusion-multiple approach for phase diagram mapping. *J. Mater. Sci.* **2004**, *39*, 3913–3925. [CrossRef]
104. Luyten, J.; De Keyzer, J.; Wollants, P.; Creemers, C. Construction of modified embedded atom method potentials for the study of the bulk phase behaviour in binary Pt-Rh, Pt-Pd, Pd-Rh and ternary Pt-Pd-Rh alloys. *Calphad* **2009**, *33*, 370–376. [CrossRef]
105. *Powder Diffraction File PDF-2*; International Centre for Diffraction Data (ICDD): Newtown Square, PA, USA, 2009.
106. Tripathi, S.N.; Bharadwqj, S.R. The Pd-Rh (Palladium-Rhodium) system. *J. Phase Equilibria* **1994**, *15*, 208–212. [CrossRef]
107. Koffyberg, F.P. Optical bandgaps and electron affinities of semiconducting Rh_2O_3(I) and Rh_2O_3(III). *J. Phys. Chem. Solids* **1992**, *53*, 1285–1288. [CrossRef]
108. Aita, C.R. Optical behavior of sputter-deposited platinum-oxide films. *J. Appl. Phys.* **1985**, *58*, 3169–3173. [CrossRef]
109. Zhensheng, J.; Chanjuan, X.; Qingmei, Z.; Feng, Y.; Jiazheng, Z.; Jinzhen, X. Catalytic behavior of nanoparticle α-PtO_2 for ethanol oxidation. *J. Mol. Catal. A-Chem.* **2003**, *191*, 61–66. [CrossRef]